Methods 223 (2024) 83–94

Contents lists available at ScienceDirect

Methods

journal homepage: www.elsevier.com/locate/ymeth

Atomic force microscope kymograph analysis: A case study of two membrane proteins

Dylan R. Weaver [a,1], Katherine G. Schaefer [a,1], Gavin M. King [a,b,*]

[a] Department of Physics and Astronomy, University of Missouri-Columbia, Columbia MO 65211 USA
[b] Joint with Department of Biochemistry, University of Missouri-Columbia, Columbia MO 65211 USA

ABSTRACT

Kymograph analysis is employed across the biological atomic force microscopy (AFM) community to boost temporal resolution. The method is well suited for revealing protein dynamics at the single molecule level in near-native conditions. Yet, kymograph analysis comes with limitations that depend on several factors including protein geometry and instrumental drift. This work focuses on conformational dynamics of difficult-to-study sparse distributions of membrane proteins. We compare and contrast AFM kymograph analysis for two proteins, one of which (SecDF) exhibits conformational dynamics primarily in the vertical direction (normal to the membrane surface) and the other (Pgp) exhibits a combination of lateral dynamics and vertical motion. Common experimental issues are analyzed including translational and rotational drift. Conformational transition detection is evaluated via kymograph simulations followed by state detection algorithms. We find that kymograph analysis is largely robust to lateral drift. Displacement of the AFM line scan trajectory away from the protein center of mass by a few nanometers, roughly half of the molecule diameter, does not significantly affect transition detection nor generate undue dwell time errors. On the other hand, for proteins like Pgp that exhibit significant azimuthal maximum height dependence, rotational drift can potentially produce artifactual transitions. Measuring the height of a membrane protein protrusion is generally superior to measurement of width, confirming intuition based on vertical resolution superiority. In low signal-to-noise scenarios, common state detection algorithms struggle with transition detection as opposed to infinite hidden Markov models. AFM kymography represents a valuable addition to the membrane biophysics toolkit; continued hardware and software improvements are poised to expand the method’s impact in the field.

1. Introduction

Membrane proteins are difficult to characterize via traditional techniques, yet they constitute ~ 30 % of proteins expressed in cells and perform critical functions. The range of activities include the efflux of pharmaceutical agents used in the treatment of diseases to the translocation of polypeptide chains in secretion pathways. Recent progress in understanding underlying molecular mechanisms comes from high-resolution crystallographic structures in various conformations [1–4]. In addition, thanks to advancements in cryo-electron microscopy (cryo-EM) [5–7], determining the structure of membrane proteins is much more commonplace [8]. However, these techniques only provide static frames of proteins which usually span a vast conformational landscape over the course of executing functional imperatives. In addition, many of the complicated processes associated with membrane proteins are dependent on stochastic aspects and environmental conditions, which are challenging to study with cryogenically preserved samples. To improve understanding of the structure and function of membrane proteins static information can be complemented by single-molecule techniques that are able to track asynchronous activities in real-time.

While several single-molecule techniques are emerging as useful tools in studying the dynamics and function of complex membrane-embedded proteins, atomic force microscopy (AFM) [9–11] has become an increasingly powerful method that allows for the collection of high-resolution spatial and temporal data. In brief, the sharp cantilever probe of the AFM gently scans across a biological sample extracting salient structural information, such as height or volume above the membrane surface, with molecular-scale (~10 Å) lateral resolution coupled with ~ 1 Å vertical resolution. The data is obtained in buffer solution, providing physiologically relevant conditions for biological macromolecules. Technical advancements to cantilevers, stage scanners, detectors, and feedback loops has allowed for AFM to reach “high speed” [12,13], making video-rate AFM imaging of biological macromolecules possible, which has led to prominent discoveries about their structure and function [14,15]. Notwithstanding these impressive advancements, conformational dynamics of membrane proteins can still be probed using conventional scanning speed AFM systems. One can utilize kymographs (trace/retrace line scan analysis, shown schematically in Fig. 1) to achieve < 100 ms temporal resolution without the need for a high-speed setup [16–19].

---

[*] Corresponding authors at: Department of Physics and Astronomy, University of Missouri-Columbia, Columbia MO 65211 USA.
E-mail address: kinggm@missouri.edu (G.M. King).

[1] Authors contributed equally

https://doi.org/10.1016/j.ymeth.2024.01.013
Received 15 September 2023; Received in revised form 9 January 2024; Accepted 10 January 2024

Our lab has utilized AFM kymograph analysis to study membrane proteins in physiologically relevant conditions. In particular, we have used the technique to probe the conformational dynamics of the general secretory, or Sec, system in *Escherichia coli*, which is the primary export pathway for unfolded polypeptides within the inner membrane [16,20–23]. Recently, we have shown that SecDF, an integral membrane protein translocation factor, experiences a higher transition rate among conformational states in the presence of translocon SecYEG [21]. While that work demonstrated how kymographs can be utilized to study membrane protein dynamics, it did not focus on factors that can affect data collection, such as instrumental drift. Drift-related artifacts are commonly the result thermal perturbations and an AFM's limited mechanical stability, but can also be a consequence of protein diffusion within the membrane during data collection in fluid. Drift rates are variable, about 2 nm/min when the instrument is allowed to settle and diffusion is minimal. In our experiments it is often higher, up to 9.5 nm/min [24,25]. Under these conditions, a typical kymograph collection time of 25 s allows for a maximum drift magnitude of 4 nm. This is a significant fraction of many proteins' lateral dimension including those studied here. One may intuit that allowing 4 nm of drift (or more) would deleteriously affect data quality. We analyzed some of these limitations while studying P-glycoprotein (Pgp), an ATP-binding cassette (ABC) transporter involved in cancer drug efflux [26,27]. We have shown through kymograph analysis that Pgp also undergoes conformational transitions at the 100 ms timescale under varying experimental conditions [25].

The conformational changes observed in both SecDF and Pgp are a result of specific domains within each protein that change their state under certain conditions (Fig. 2). Structures of SecDF in various conformational states showcase a dynamic periplasmic domain known as the P1-head/base of SecD [28]. Structural and functional analyses have suggested that the large P1 domain of SecD plays a critical role in stimulating precursor protein transport in a manner dependent on proton motive force (PMF) [28–30]. In the absence of PMF, SecDF conformations tend to fluctuate between the super membrane-facing form (Super F) and membrane-facing form (F). AFM assays have helped obtain salient information that complements reported crystal structures (Fig. 2, bottom row). One can use software to objectively extract metrics such as height and volume of individual proteins [31]. These experimental images may not always resemble the exact geometry of a crystal structure, due to thermal fluctuations, a consequence of imaging the protein in a near-native fluid environment. Yet, even without matching geometries, the measured height of an individual protein can often be used to assign its orientation in the membrane and conformational state.

Pgp conformational states can be described as inward-facing (IF), in which the two nucleotide binding domains (NBDs) are separated, and the drug-binding sites are exposed to the cytosol, or outward-facing (OF), in which the NBDs are closely associated, and the transport channel is open to the extracellular space. The IF conformation has a large amount of variability, depending on the degree of association for the NBDs, and extreme cases of the IF conformation have been reported as well [27,32,33]. The dynamics of the NBDs are thought to be coupled with the ATP hydrolysis cycle [34,35].

We present a case study of AFM kymograph analysis applied to two distinct membrane proteins, Pgp and SecDF (Fig. 2). To closely mimic physiological conditions these proteins were studied in fluid lipid bilayers. Both proteins possess dynamic behavior that is captured at the 100 ms timescale of conventional (i.e., non-high speed) AFM hardware. SecDF exhibits conformational dynamics primarily in the vertical direction whereas Pgp exhibits a combination of lateral dynamics and vertical motion. We address issues such as reliability and repeatability of kymograph experiments; these include protein orientation, instrument noise, and mechanical drift. Simulations of AFM data were utilized to enhance understanding of these factors and quantify errors. The overall shape and conformational states of the two model proteins evaluated in this study differ significantly. We demonstrate how a protein's geometric structure reveals itself through kymograph analysis, and how artifacts can emerge. This work showcases both the utility and potential pitfalls of kymograph analysis for studying membrane protein dynamics. In certain situations, minute changes in protein orientation with respect to the tip trajectory substantially complicates kymograph data and analysis.

2. Materials and methods

2.1. Sample preparation

To prepare proteoliposomes, lipid stock (Avanti Polar Lipids) suspended in chloroform in a glass tube was dried with argon gas to create a film (details provided in [36]. For SecDF, we utilized *E. coli* Polar Lipid Extract and for Pgp we used 80 % w/v *E. coli* Total Lipid Extract with 20 % w/v cholesterol. The tube was then placed in a vacuum chamber and evacuated overnight via a dry roughing pump (Edwards). Following swelling in buffer, the lipids were extruded 25–30 times through filters (Whatman, Product #WHA800309) to create vesicles. The effective size of the liposomes was evaluated via dynamic light scattering [27,37]. The swelling buffer was the same as the imaging buffer (described below). Each batch of lipid stock was quantified using an appropriate assay, such as the Bartlett assay [38]. The proteins were purified following established protocols and reconstituted into liposomes to be imaged via AFM [21,25]. Proteoliposome suspensions were stored at −80 °C.

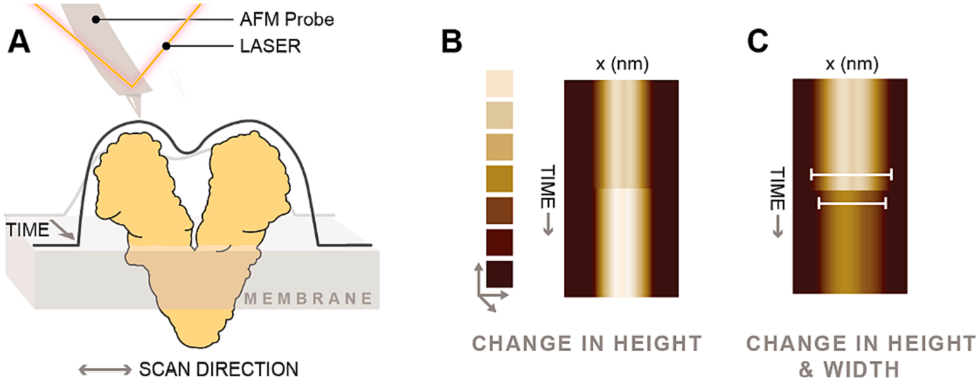

Fig. 1. (A) A cartoon depicts the kymograph technique, in which the AFM probe scans in one dimension over time to build up a sequence of line scans reflecting membrane-external protein topography. (B) Fluctuations in protein conformation can be detected as changes in z-dimension (a change in line scan height). (C) More generally, changes in height are accompanied by changes in the lateral dimension (a change in line scan width).

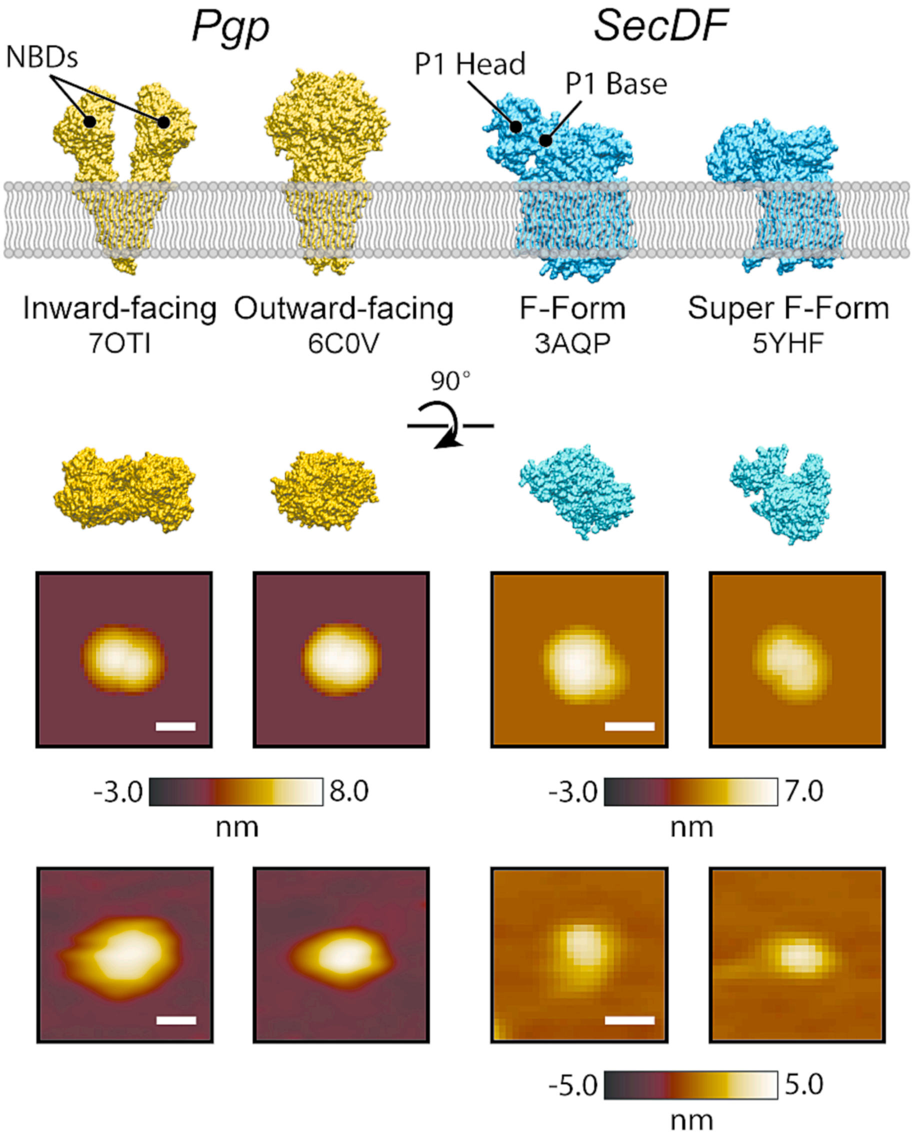

Fig. 2. The two proteins of interest shown in different conformations. P-glycoprotein (Pgp, yellow) is an ABC transporter that works as a drug efflux pump; it is often expressed in cancer cells, resulting in cancer drug failure. Reported structures of Pgp exhibit large scale conformational changes due to its two nucleotide binding domains (NBDs). SecDF (blue) is a translocation factor that is involved in polypeptide secretion across bacterial membranes. Current discussion about the function and dynamics of SecDF focuses on the motion of the P1 Head and Base domains in the periplasm. Simulated AFM images are provided below each crystal structure. The bottom row shows representative experimental images of each state. Various software can be used to extract the heights of individual proteins and compare them to simulated images [30]. The scale bars are 10 nm. (For interpretation of the references to color in this figure legend, the reader is referred to the web version of this article.)

2.2. Surface preparation

Preparing AFM samples requires a supporting surface. For imaging on mica, the disc was attached to metal AFM specimen discs (TED PELLA, Product # 16208) with a Teflon separator to prevent spillover. Care was taken to uniformly distribute the epoxy between the mica and Teflon to prevent air bubbles under the surface. Prior to depositing a biological sample, the mica disc was cleaved to ensure a uniform surface for AFM imaging. In the case of glass, we utilized coverslips purchased from Corning (18 × 18 mm, No. 1.5, catalog #: 2850–18). These coverslips were prepared via KOH etching, as described in [39]. Over time surfaces can lose their hydrophilicity [40]. So, immediately before experiments, coverslips were plasma cleaned (Harrick Plasma PDC-001) in oxygen for 10 min at 250 mTorr using ~ 30 W forward RF power. The glass was then affixed to a Teflon-covered metal disc with epoxy.

2.3. AFM imaging

Aliquots of proteoliposome stock were removed from −80 °C and thawed. The sample was diluted in imaging buffer (20 mM Hepes, 100 mM NaCl, 5 mM $MgCl_2$ pH 7.3 for Pgp and 10 mM Hepes, 30 mM KCl, 1 mM $MgCl_2$, 1 mM Tris(2–carboxyethyl)phosphine pH 7.6 for SecDF) to ~ 80 to 100 nM. Then 100 μL was added to the prepared mica or glass surface. Samples were incubated at room temperature for 30 min to allow proteoliposomes to rupture and spread on the surface. Excess proteoliposomes were removed by rinsing 5–6 times via buffer exchange (100 μL volumes exchanged with a pipette). We used 100 μL of buffer solution for AFM imaging of either protein. AFM data were collected in tapping mode (Cypher, Asylum Research) with BioLever mini tips (Bruker, $k \sim 0.1$ N/m, $f_o \sim 25$ kHz in fluid) and tip-sample forces maintained below ~ 100 pN. Kymographs were collected with scan rates of 6.5 to 11.2 Hz. In the case of Pgp, 5 mM ATP-γ-S was added to the sample after imaging apo-Pgp. Following a 10 min incubation period in the AFM (at $T \sim 35$ °C), images were collected in the same nominal area as the apo condition.

2.4. Kymograph analysis

To extract precise topographical information from AFM kymographs a version of the Hessian blob algorithm [31] modified for linear features [36] and implemented with custom software (Igor Pro 7; WaveMetrics) was used. In this method, the image skeleton is extracted. The lateral boundaries, central backbone, and maximum height pixel for each line within the kymograph are then extracted. For kymographs that exhibited lateral drift perpendicular to the scan direction, the data was fit to a line to enable drift subtraction from the trace. Traces of maximum height versus time were analyzed by the STaSI state detection algorithm [41] or the infinite Hidden Markov model (iHMM), both implemented in MATLAB (MathWorks) [19]. An optimal number of states was determined for each kymograph by considering the simplest model, which gives the least fitting error (minimum description length) [42]. Kinetics were deduced by counting transitions between states.

2.5. Simulation of AFM images and kymographs

AFM images of Pgp were simulated from the crystal structures 7OTI [43] for the IF state and 6C0V [44] for the OF state. For SecDF, we utilized crystal structures 5YHF [45] and 3AQP [28] for the Super-F and F forms, respectively. In the structures, each atom was modeled as a sphere with van der Waals radius [46]. Membrane placement was determined using the Orientations of Proteins in Membranes (OPM) database [47], with 4.8 Å added to account for the lipid head groups. The tip geometry, deduced from comparison between experimental and model data, was approximated by two overlapping spheres, the apex sphere having a 40 Å radius and the base sphere having an 80 Å radius [48]. The images had a lateral spacing of 10 Å per pixel. Taking individual line scans across the images and stacking them in “time” yields simulated kymographs (Fig. 3). These scans were collected for 0° to 165° in 15° increments. For each angle, displacement from the center of mass was also simulated in 1 nm steps until the model tip reached the edge of the feature. Line scans were each stacked in “time”, alternating twice with a dwell time of 64 time units for each state. The final result was a

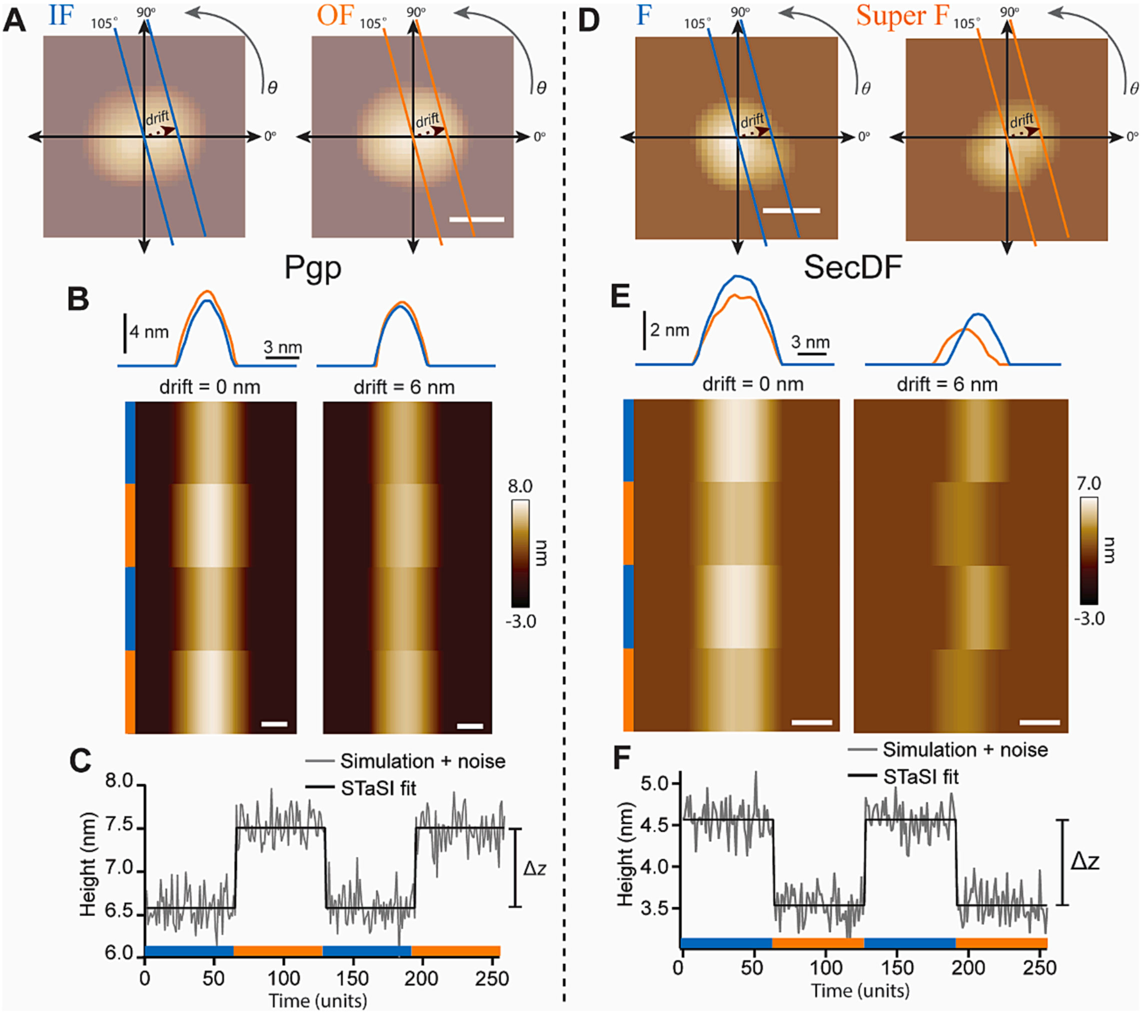

Fig. 3. Kymograph simulations. (A) Kymographs are simulated from Pgp crystal structures by taking line scans across simulated AFM images. The orange and blue scan lines shown are at an angle of 105° with 0 nm and 6 nm displacement from the center of mass of each image. Two states are used: the IF conformation (blue) and the OF conformation (orange); the 10 nm scale bar applies to both images. (B) Line scans of the IF and OF states are displayed above each kymograph simulated at 105°. The left panel displays a kymograph at the center of mass (drift = 0 nm), and the right panel displays a kymograph with a drift of 6 nm. Line scans for each state are stacked for 64 time units each and alternated twice; this results in a kymograph with a 256 time unit duration exhibiting 2 states and 3 transitions. (C) The maximum height pixels are extracted from the kymograph simulated at 105° and 0 nm. AFM-typical Gaussian noise ($\sigma = 2$ Å) is added. The STaSI algorithm fits the simulated data with states and identifies transition points. The vertical height difference between states, Δz, is shown to the right of the graph. (D-F) show analogous analysis for SecDF, using structures for the F form (blue) and Super-F form (orange). Data in (A-C) adapted from Ref. [26]. (For interpretation of the references to color in this figure legend, the reader is referred to the web version of this article.)

kymograph with two states and three transitions, lasting 256 time units. To generate single-dimensional traces of the kymograph backbone, the maximum pixels were extracted, and Gaussian noise was added. Gaussian noise was generated using a Box-Muller algorithm and had a standard deviation of 2 Å (Fig. 3C, F).

3. Results

3.1. Overview of kymograph analysis

The standard process for acquiring an AFM image involves the cantilever tip raster-scanning over a surface in two dimensions, rendering a topographic map of a sample. One can disable the “slow scan” of the raster pattern to acquire kymographs for line-scan analysis. This converts one of the two spatial axes to a temporal axis, or $Z(x,y)$ to $Z(x,t)$ (Fig. 1). Analyzing the resulting kymographs is useful in probing the dynamics of biological macromolecules across time and can be used to evaluate conformational changes under different experimental conditions, such as the presence of a genetic mutation, a small therapeutic molecule, or another ligand. The data can be analyzed using specific software that is suitable for extracting transition points in one-dimensional data, such as the STaSI algorithm [41].

Fig. 4 shows kymographs for the two model membrane proteins employed in this study. While crystal structures help in describing distinct conformational states of membrane proteins, kymographs are useful for visualizing the intermediate states that may exist in between the structural states. Here, changing dynamics of SecDF are revealed upon a domain-specific deletion, while Pgp dynamics are probed in the presence or absence of a non-hydrolyzable ATP analog (ATP-γ-S). Both of these conditions induce a decrease in dynamics, as the P1 region of SecDF is the mobile domain and ATP-γ-S halts the hydrolysis cycle of Pgp, which is a highly dynamic protein even in the apo state

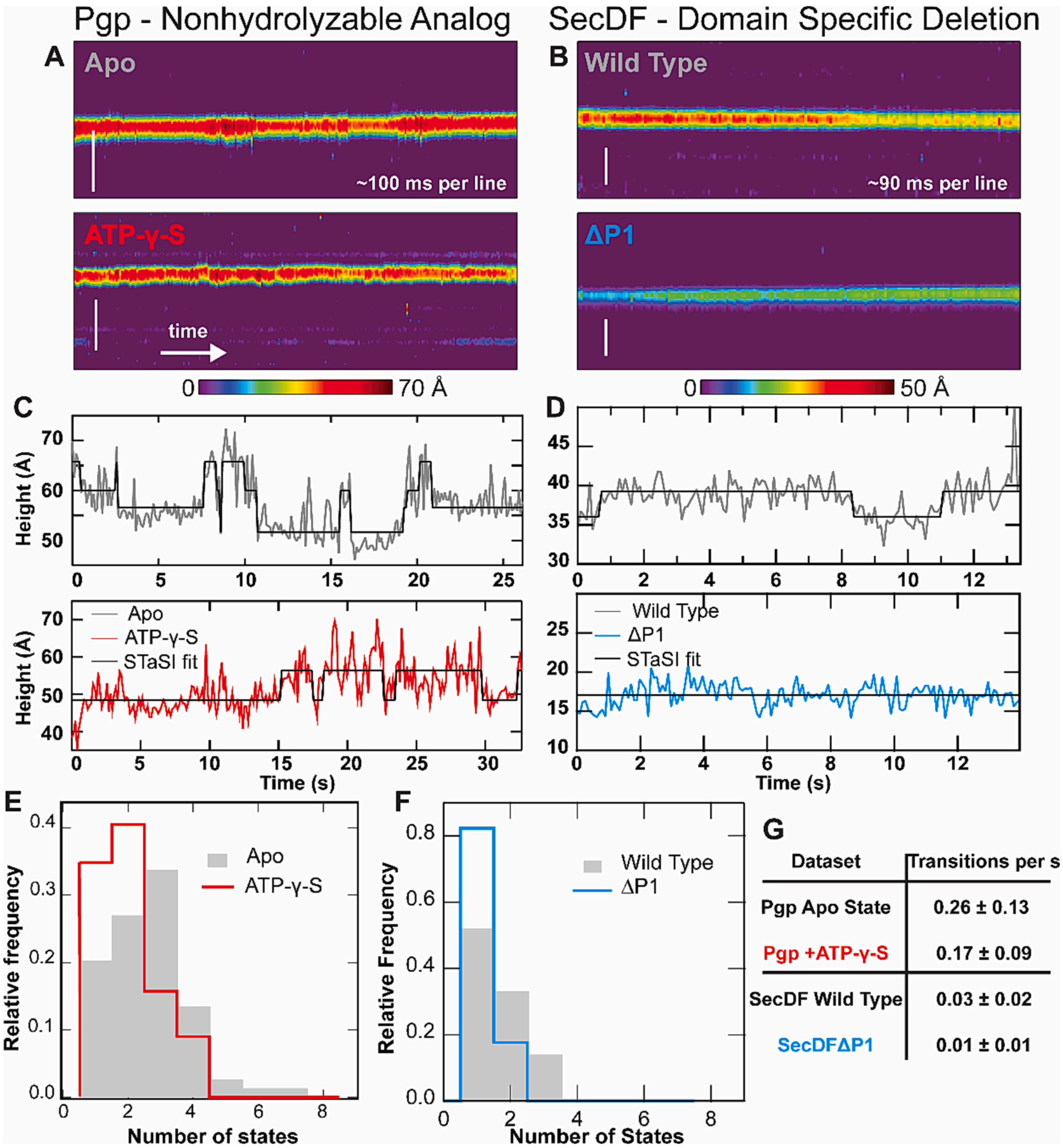

Dataset	Transitions per s
Pgp Apo State	0.26 ± 0.13
Pgp +ATP-γ-S	0.17 ± 0.09
SecDF Wild Type	0.03 ± 0.02
SecDFΔP1	0.01 ± 0.01

Fig. 4. AFM kymographs reveal changing conformational dynamics with experimental conditions. (A) Kymographs of Pgp in both Apo and non-hydrolyzable ATP-γ-S conditions. (B) Kymographs of wild type SecDF and SecDFΔP1, in which the periplasmic P1 region is deleted. (C) and (D) show the maximum height of each line-scan across the kymographs depicted in (A) and (B), respectively. Each trace contains both the raw height profile, as well as the fit by STaSI (black lines). The raw kymographs, especially SecDF in (B), show drift, which provides motivation for studying this artifact further. (E), (F) Histograms of the number of states detected highlight how each protein exhibits a decrease in the number of states due to either (E) ATP-γ-S addition (Pgp) or (F) P1 deletion (SecDF). (G) The average transitions per second of active kymographs for each data set is reported (±standard deviation). Data adapted from Refs. [21,26].

[25,33,49,50]. The kymographs span $\geq$ 20 s, enabling detection of multiple transitions. In each case, changes in the most probable number of states were detected via STaSI analysis. These states were extracted in an objective manner by considering the simplest model, which gives the least fitting error (minimum description length) [42]. We also see that in addition to the number of states, the transition rate changes when the experimental conditions are altered for both proteins (Fig. 4E-G). These data demonstrate how AFM kymograph analysis can directly probe membrane protein dynamics in near-native conditions.

3.2. *Simulating kymographs*

While kymograph analysis is enticing in the context of spatial–temporal resolution, it is not without its drawbacks, and those should be discussed and analyzed as well. Kymograph data is limited by several factors emanating from experimental constraints. The concerns include drift in the mechanical loop between the AFM tip and the sample stage, noise in the data, which is acquired in fluid at (or near) room temperature, the angular orientation of the protein with respect to the tip scanning axis and the ability to initiate a kymograph on, roughly, the center of mass of the protein. Simulated kymographs are helpful for quantitatively analyzing these concerns.

A common artifact in AFM measurements is the gradual shift from the original reference point, in this case, the center of mass of the protein. We will henceforth refer to this displacement as simply "drift," and the rate of change as the "drift rate." We have demonstrated how this can be visualized during kymograph collection (Fig. 4B). Drift can obscure detectable conformational transitions [25]. To assess the effect of this potential artifact for each protein, simulated AFM images were generated using relevant crystal structures of two distinct conformational states (See Section 2: Materials and Methods). Each simulated kymograph sampled two states and three transition points, with an equal number of time steps in between each state. Fig. 3 shows this analysis applied to Pgp and SecDF. Variations in distance from the center of mass and scan angle elucidate the effects of drift-induced artifacts during kymograph analysis.

3.2.1. *Protein geometry affecting lateral drift results*

One question that can be addressed from simulated kymographs is the effect of instrument drift on the ability to measure transitions between distinct protein conformational states. Transition detection (see Fig. 3C, F) is largely dependent on the signal-to-noise ratio (S/N), where the signal is the measured height difference between conformational states (Δz). Fig. 5 demonstrates how Δz varies with lateral drift for the two model proteins, assuming the user has no knowledge of the protein's orientation (Fig. 5A, B). During operation, visual identification of lateral drift is easy to detect, due to the height change as the tip "falls off" the protein. Assuming equal probability of protein orientations, we generated a two-dimensional histogram of possible Δz's resulting from lateral drift to better visualize the degeneracy resulting from obscured protein

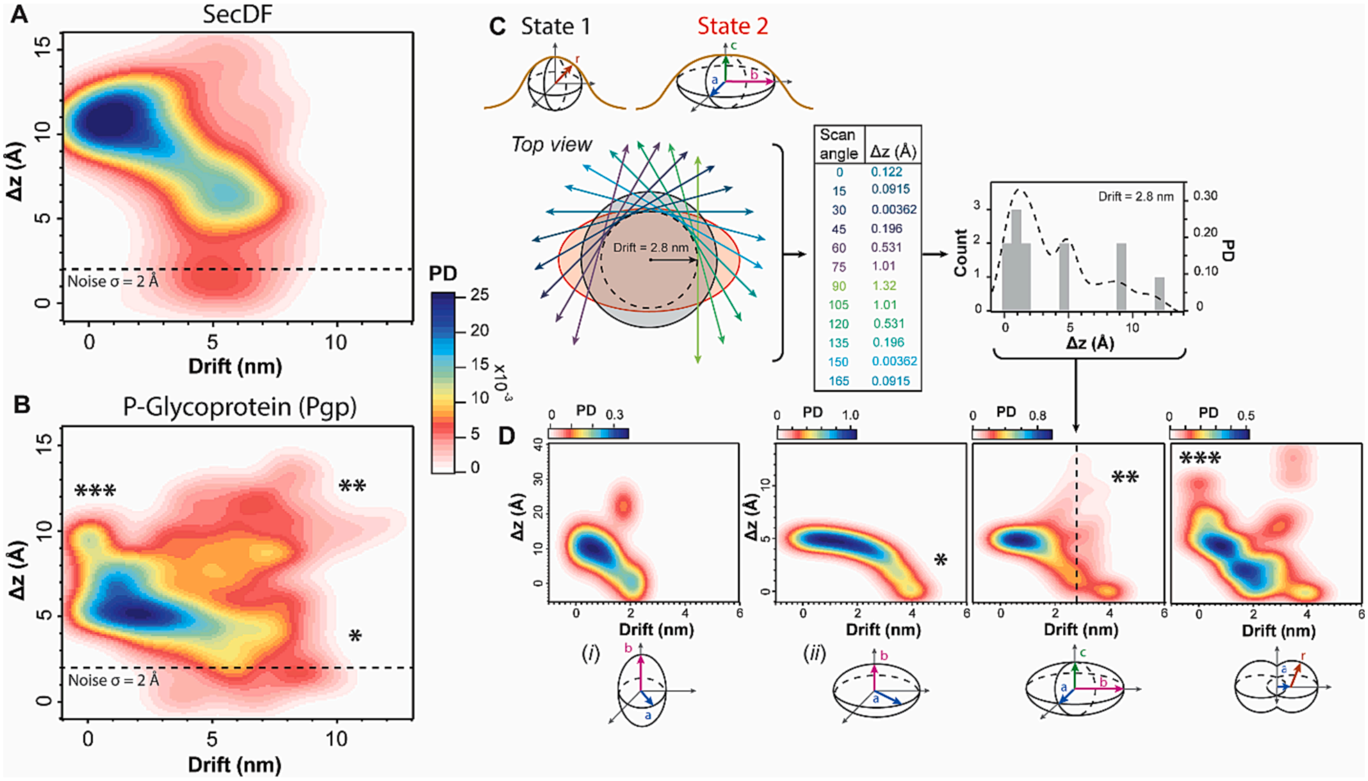

Scan angle	Δz (Å)
0	0.122
15	0.0915
30	0.00362
45	0.196
60	0.531
75	1.01
90	1.32
105	1.01
120	0.531
135	0.196
150	0.00362
165	0.0915

Fig. 5. The effect of lateral drift on height change (Δz) recorded in a kymograph. (A), (B) The height difference Δz resulting from all scan angles is plotted in a heat map versus lateral drift for SecDF and Pgp, respectively. The vast majority of Δz's are above the 2 Å noise level (dashed line) for both proteins. (C) A demonstration of how these heatmaps are generated is shown using simple geometries, a sphere for State 1 followed by an ellipsoid for State 2. Gold lines approximate the topographical envelope imaged with an AFM tip. Scan lines of simulated AFM images are taken with different angles and drift (drift = 2.8 nm shown here), similar to previous simulations. The Δz from State 1 to State 2 is calculated for each scan angle. A histogram of possible Δz's for a lateral drift of 2.8 nm is shown (right), with a smoothed probability density (PD) distribution overlaid. An arrow indicates where this PD distribution projection would appear on the 2-dimensional heatmap if State 2 is an ellipsoid. (D) In this way, the complexities of the heat maps in (A) and (B) can be recapitulated by simplifying states into basic geometries. For SecDF, the dominant trend is decreasing Δz with drift. As before, we approximate State 1 with a sphere, and a prolate spheroid for State 2 (i). The resulting Δz vs lateral drift heat map correlates with trends observed in (A). For Pgp, the complex behavior can be isolated into three trends: (*) Δz decreasing with drift, (**) Δz increasing with drift, and (***) bimodal Δz at the center of mass. States are again simplified into a sphere for State 1 followed by three different geometries for State 2 (ii): an oblate spheroid, an ellipsoid, and two overlapping spheres. The resulting Δz vs lateral drift heat maps correlate with behaviors observed in (B). The false color scale bars are unitless, normalized PD. Data adapted from Refs. [21,26].

orientation. An example of the different Δz's that can arise with a single lateral drift value is demonstrated for a lateral drift of 2.8 nm for simplified geometric states (Fig. 5C). This is expanded into two-dimensional histograms for all lateral drifts considered. For SecDF and Pgp, these heat maps display the complex distribution of Δz's versus the imposed magnitude of drift in the simulated kymographs (Fig. 5A, B).

Structures have suggested that SecDF conformational dynamics are centered around the primarily vertical motion of the P1-Head domain [28,30]. In contrast, significant lateral and vertical changes are expected in Pgp conformations due to the motion of two large nucleotide binding domains (NBDs). For SecDF, the majority of height transitions occur above the noise level of 2 Å (S/N > 1). Furthermore, Fig. 5A shows the SecDF Δz distribution trending downward as the drift increases. Pgp exhibits large lateral displacements and azimuthally dependent maximum height. These factors lead to a more complex Δz versus drift landscape (Fig. 5B). In particular, a multi-modal distribution of height differences extending beyond 7 nm of lateral drift is observed for Pgp.

Basic geometric shapes can be used to guide interpretation of the complex Δz versus drift heat maps shown in Fig. 5A&B. A single sphere (Fig. 5C) approximates "State 1" for both model proteins. In particular, the SecDF sphere (representing the super F form) has a radius, $r = 1.8$ nm, whereas the Pgp sphere (representing the closed "Inward-Facing" state) has $r = 3.8$ nm. "State 2" can be approximated in a number of ways, such as the ellipsoid shown in the example in Fig. 5C. Just as with the protein crystal structures, AFM images may be simulated and scanned at different angles. The Δz between the two states can then be extracted and a histogram made of the distribution of Δz values for all angles with a particular lateral drift (2.8 nm in this example). To understand the heat map resulting for SecDF, "State 2" (the F form of SecDF) was approximated as a tall prolate spheroid ($a = 1.6$ nm, $b =$

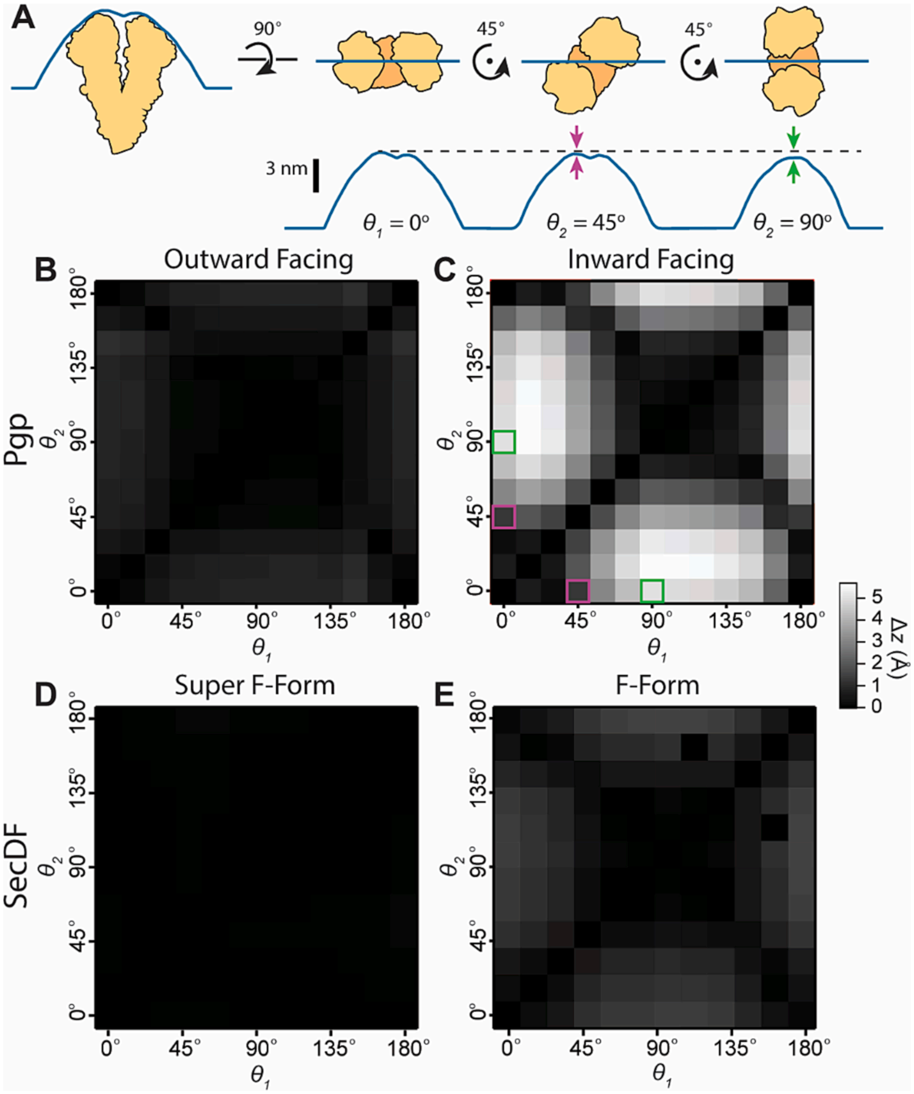

Fig. 6. Rotational drift can produce artifactual transitions. To demonstrate the effect of rotational drift, height differences, Δz, are calculated for rotations of each protein. (A) A cartoon demonstrates example rotations from 0° to 45° and 90° for the IF conformation of Pgp and the resulting Δz which arises from rotational asymmetry (pink and green arrows respectively). The Δz is plotted for each angular displacement for the OF (B) and IF (C) conformations of Pgp. A matrix is built for the Δz between a reference angle's line scan and subsequent rotations. The axes correspond to the possible scan angle we chose for our kymograph analysis. Each pixel in the matrix represents the difference in feature height relative to the membrane between two scan angles. For example, the 0° to 45° and 45° to 0° pixels are highlighted in pink (C), corresponding with panel A. A second example is shown for 0° to 90° and 90° to 0° (green). All line-scans used here are along the center of mass for the protein. No rotations resulted in a detectable change for the OF conformation. A detectable change is defined as a value for Δz above the assumed noise level ($\Delta z > 2$ Å). In contrast, several in the IF conformation were above the noise level (data scale displayed to the right of the panels). For comparison, the same analysis was applied to simulated structures for SecDF in the Super-F (D) and F (E) conformations. In both cases, no changes were detectable above the noise level. Data in (A-C) adapted from Ref. [26]. (For interpretation of the references to color in this figure legend, the reader is referred to the web version of this article.)

2.35 nm), in which b corresponds to the height of the relevant crystal structure and was calculated such that the feature volume was conserved. Though based on simple representations, the resulting Δz versus drift heat map (Fig. 5D (*i*)) captures the main features of the SecDF data (Fig. 5A). To understand the Pgp heat map, we represented the open "Outward-Facing" state using geometries of increasing complexity: an oblate spheroid ($a = 3.9$ nm, $b = 3.55$ nm), an ellipsoid ($a = 3.09$ nm, $b = 5$ nm, $c = 3.55$ nm), and two overlapping spheres ($r = 3.55$ nm, $a = 2$ nm), representing the increased separation of the NBDs in the open state. These geometries recapitulated some of the main features of the observed heat map textures for Pgp (compare *, **, & *** in Fig. 5D (*ii*) with Fig. 5B). To summarize, basic geometric modeling gives insight to the nature of the height difference between conformational states (Δz) versus drift landscapes observed for both SecDF and Pgp.

3.2.2. *Rotational drift*

The aforementioned examination of lateral drift effects was performed with static, simulated images of a membrane protein. The static nature of these images implies that the protein is torsionally constrained. This is an assumption that may be suitable for 2D arrays of densely packed proteins like bacteriorhodopsin, but may not carry over to sparse distributions of individual membrane proteins in a bilayer membrane such as those employed in the current study. During AFM imaging and kymograph collection, one cannot easily control the orientation of a diffusing protein with respect to the trajectory of the scan. If a protein undergoes an angular displacement during kymograph collection, known as "rotational drift," it can lead to false positives in state detection [25]. If possible, one should examine the potential changes in height due to rotation, by examining line-scans across simulated AFM data. Proteins with azimuthally dependent maximum height can lead to erroneous state detection (Fig. 6). We can demonstrate this by comparing the difference in heights determined with different scan angles on the same crystal structure. Pgp is a key example of this; the Inward-Facing conformation of Pgp exhibits certain values of angular displacement that lead to height transitions above the 2 Å noise level (Fig. 6A, C), while the Outward-Facing conformation does not (Fig. 6B). Conversely, neither conformational state of SecDF exhibits false transition heights (Fig. 6D, E), on account of minimal azimuthal height dependence.

3.2.3. *Kymographs of protein width vs. Height*

Since certain angular displacements produce detectable changes in maximum height, we sought to determine if other physical metrics of a protein's structure could be used when probing conformational dynamics. In this context, we turn to the protein's width, which could also vary depending on the protein's rotational orientation. We applied our

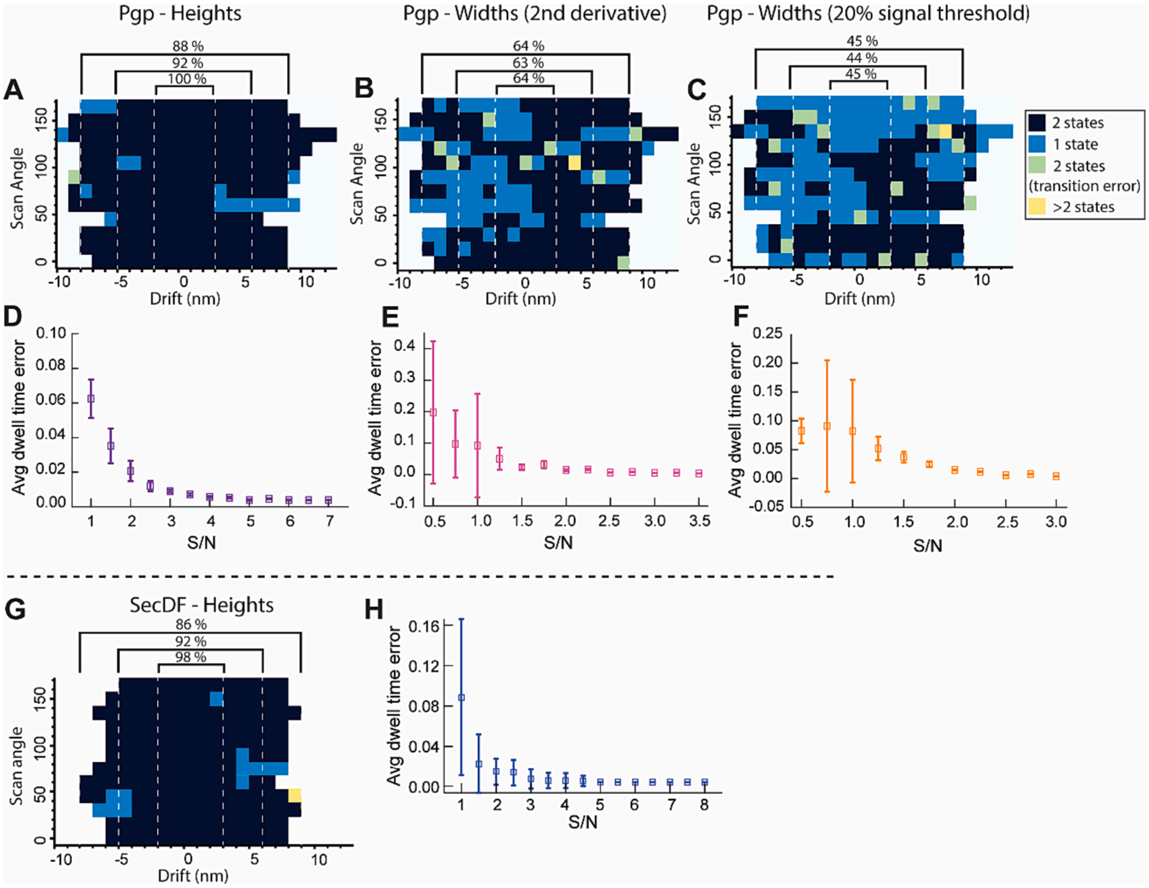

Fig. 7. Accuracy of state and transition detection varies with measured quantity. The graphs (A-C, G) display the number of states detected for scan angle and drift from protein center of mass (0 nm). We applied the STaSI algorithm to detect states for the height and width transitions. An accurate state detection results in 2 states (black). There are 3 possibilities for inaccurate detection: 1 state is detected (light blue), 2 states with more than 3 transitions are detected (green), or more than 2 states are detected (yellow). The detection accuracy for certain margins, calculated as the number of accurate state detections per number of kymographs analyzed within that margin, is displayed above each plot. (A) The data for Pgp demonstrates that the majority of height transitions are accurately detected even in the presence of substantial drift. (D) The relative deviation from the expected dwell time (64 time units) is quantified for the data shown in (A) as a function of signal to noise (S/N) ratio (error bars = σ). Additionally, we applied the same protocol to kymographs generated from the width transitions for Pgp. Width was calculated via (B) the 2nd derivative test and (C) the width at 20 % of the signal threshold. Each case resulted in increased transition errors. (E) and (F) show the relative dwell time error for both width methods. (G, H) The analysis was repeated for height transitions of SecDF. Data in (A, D) adapted from Ref. [26]. (For interpretation of the references to color in this figure legend, the reader is referred to the web version of this article.)

kymograph simulation approach to the lateral width of Pgp crystal structures, with adjustments made for the noise difference in the lateral dimension. Previously, a 2 Å Gaussian noise source was employed for vertical noise simulations. Using experimental data, we determined an appropriate Gaussian noise source had a standard deviation of 14 Å and was limited by the pixel resolution of the image, in this case a quantization of 10 Å. We performed drift analysis to determine the metric's reliability. Fig. 7A-F shows data for Pgp. The plots demonstrate cases in which there was an error in state detection: 1 state is detected, more than 2 states are detected, or more than 3 transitions are detected. These various errors are based upon the construction of simulated kymographs in Fig. 3. Lateral dimensions of the protein protrusions detected via AFM are subject to tip convolution, so the measured width in a kymograph will not always reflect the true width of the protein, as opposed to the maximum height. Therefore, one must be careful in what method is used to extract kymograph width. Here, we calculated the width using two different methods: (*i*) the 2nd derivative test, and (*ii*) the calculated width at 20 % of the height signal threshold. For both width measurement methods, the success rate of correct state and transition detection decreases greatly. This rate represents the percentage of kymographs in each dataset that accurately determined 2 states and 3 transitions. For comparison, the success rate for the height metric decreased from 100 % to 88 % depending on the level of drift and was 92 % if all kymographs were considered (Fig. 7A). In contrast the success rate remained stable with instrumental drift for width analysis and was 64 % overall for the 2nd derivative test and 44 % for the signal threshold method (Fig. 7B, C). Additionally, in cases where the correct number of states and transitions were detected, the dwell time was less accurate for width detection (Fig. 7D-F). It should be noted that the regions in which state detection was most accurate were those in which the line-scan was over the NBD regions in Pgp. For SecDF, which does not undergo a large lateral displacement, only the heights were scrutinized (Fig. 7G, H). The success rate of transition detection for SecDF height measurements was 93 % overall. As with Pgp, dwell time errors were relatively small for SecDF and increased as the S/N < 2.

4. Discussion & conclusions

AFM-based kymograph analysis is well suited for studying membrane protein dynamics in real time and in fluid. The method complements common structural techniques such as crystallography and cryoEM that provide static snapshots. However, the method is not devoid of pitfalls. It is important to illuminate sources of error and quantify error magnitudes. Static structures shed light on the conformational states of both SecDF and Pgp and provide an important framework for interpreting single-molecule AFM data. Challenging questions about protein conformational dynamics can be addressed by correlating kymograph measurements with changes in experimental conditions.

Lateral drift commonly occurs during kymograph acquisition. When the drift direction is parallel to the scan direction, it is innocuous (Fig. 8A). Perpendicular drift, however, results in protein height changes (Fig. 8B). Although slow drift rates relative to the scanning speed reduce the probability of artifactual transition detection due to drift, these may still occur. Additionally, drift may eventually lead to a loss in transition detection accuracy depending on the displacement of the scan from the center of mass. Rotations in the protein may also cause false transition detection if the angular displacement is sufficient to produce a signal change above the noise and occurs faster than the scanning speed.

SecDF, in conjunction with other membrane proteins, is thought to interact with unfolded polypeptides as they enter the periplasm via the P1-head domain [28,30]. Since the P1 domain occupies a large conformational space, we utilized AFM to demonstrate how the level of SecDF's dynamics shift downward when the P1-head is not present during an experiment. These results, coupled with previous kymograph data in which SecDF is interacting with the Sec translocon SecYEG [21], give a glimpse of basal-level dynamics of this critical membrane protein complex in *E. coli*.

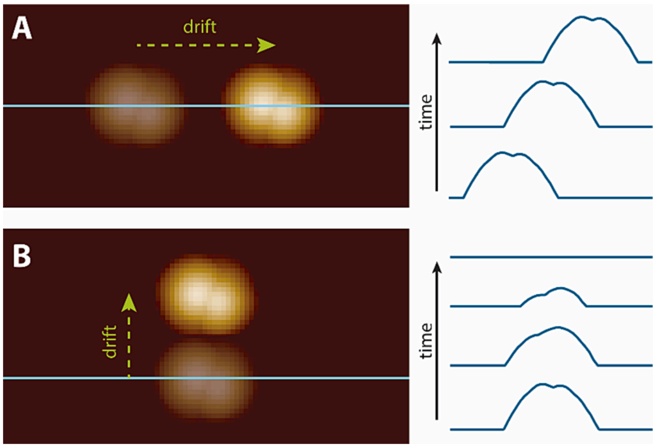

Fig. 8. Drift directionality. (A) Drift along the kymograph scanning axis (shown in the left panel) changes the feature location on the individual line scans (right panel) but does not reduce transition detection confidence as the tip still scans over the apex of the protein. (B) Drift perpendicular to the kymograph scan axis results in a change in height due to the displacement of the protein apex, therefore reducing confidence in transition detection. Data adapted from Ref. [26].

Kymograph analysis was also used to probe the dynamics of an ABC transporter. We studied the implications of Pgp binding ATP-γ-S, a non-hydrolyzable ATP analog [25]. This analog is thought to act as a plug during the hydrolysis cycle, trapping Pgp in a specific conformational state [51,52]. The results support this claim, as reduced kinetics and transition rates were observed in kymographs of Pgp in the presence of ATP-γ-S.

The spatial/temporal resolution in kymograph analysis is often dependent upon the mechanical limitations of the AFM, such as instrument noise and drift. Previous research has shown that drift in certain lateral dimensions during kymograph acquisition causes loss in the S/N, which can skew relevant data [53]. By simulating kymographs of both SecDF and Pgp in distinct conformational states (Fig. 3), we demonstrate the effect of protein geometry when lateral drift is present during AFM kymograph collection. For proteins exhibiting relatively simple geometric changes between conformational states, such as SecDF in the absence of its binding partners or PMF, the transition height tends to decrease with greater drift from the center of mass. At the same time, a majority of transition heights remained above the typical noise level of AFM experiments. Using simple geometric shapes (Fig. 5), we qualitatively described the change in conformation as a sphere whose height is stretched upward in the z-direction, with a slight width reduction to account for volume conservation. When a protein is azimuthally asymmetric and exhibits significant geometrical changes in the direction perpendicular to the membrane normal, as in Pgp, the relationship between transition height and drift can becomes multimodal. To recapitulate different regions of the conformational landscape, the Δz versus drift plot for Pgp requires additional model geometries. Nevertheless, we show that one can still detect the majority of transitions between states above the noise level.

While lateral drift is something that can be taken into account during kymograph acquisition, one must also consider the rotational freedom that membrane proteins may exhibit (Fig. 6). Membrane proteins can undergo rapid rotational diffusion in native membrane conditions [54,55]; previous results, both in the form of experimental and computational data, indicate that the rotational diffusion coefficient for membrane proteins is on the order of 10^5-10^7 rad^2/s [56–58]. In the absence of constraints, our data demonstrates that the percentage of erroneous states detected above the noise level are higher when the protein's geometry gives rise to a more complex AFM profile, as in Pgp. However, various environmental factors can impose torsional constraints on a protein and reduce angular motion, such as interactions with the membrane or with other membrane-bound components or with the supporting surface. In addition, one can expect a protein to experience reduced rotational drift if it has more than one point of contact with the surface. Since the interfacial space between the membrane and the supporting surface is small, about 1 nm [59], it is likely that multiple contact points will be achieved for larger membrane protein protrusions such as those studied in the this work.

While one can extract salient information about protein conformational dynamics by studying kymograph heights, it becomes more of a challenge when attempting to use the lateral dimensions or width of a membrane protein, even if there is a large change in width (Fig. 7). For the width of Pgp kymographs, we demonstrate that the likelihood of erroneous state and/or transition detection increased when compared to using height as the metric across multiple width calculation methods (Fig. 7B, C). These complications are largely due to tip convolution effects, which occur when the dimensions of an object are smaller than the dimensions of the tip; this is generally the case for proteins and nucleic acids. There are a range of techniques that one can use in order to combat convolution in AFM images and, by extension, kymographs [60–62]. Although we have shown that probing the lateral dynamics of Pgp gives rise to errors, there are still cases in which kymograph widths can be utilized effectively to probe biophysical questions. For example, SecA, the peripheral ATPase of the Sec system, has been shown to occupy a greater lateral conformational space in the presence of ATP [16]. Extended and compact conformations of this protein could be distinguished from kymograph analysis. This prompts future questions as to the degree to which a protein is embedded in the membrane (i.e., peripheral or transmembrane) effects artifacts during kymograph acquisition.

Analyzing AFM kymograph dynamics generally consists of applying a state-finding algorithm for quantifying kinetic parameters, such as the transition rate, across all data. In this work, we highlighted results that utilized the STaSI algorithm [41], which was developed for single molecule FRET measurements, but can be utilized for any single-channel piecewise continuous signal. While STaSI is a parameter-free analysis that outputs the optimal number of states for each kymograph trace, it is not without shortcomings. Our study shows that for simulated transitions in both heights and widths, STaSI can erroneously detect either the wrong number of states or wrong location of transition points (Fig. 7) [25]. In addition, STaSI is unable to account for traces that have apparent lateral drift, and data must be manipulated beforehand to subtract this drift out (see Section 2: Materials and Methods).

Pushing beyond STaSI, recent progress has been achieved using infinite Hidden Markov models (iHMM). This is an extension of typical HMM analysis on single-molecule data that makes use of Bayesian nonparametrics to avoid pre-specifying the number of states (in this respect it is similar to STaSI) [63,64]. Some programs have used this approach to better account for lateral drift in kymograph data, coupling the iHMM to a slow-evolving control process that accounts for drift [65,66]. When we applied one of the aforementioned programs, known as ICON [65], to our simulated kymograph data, we were able to detect transitions in certain traces that weren't previously detected with STaSI (Fig. 9). The example demonstrated in Fig. 9 has a S/N of 0.75, whereas any trace with S/N < 1 had erroneous transition detection with STaSI. While we have not rigorously compared STaSI detection versus ICON, clearly iHHM modeling represents a step forward in analyzing single-molecule data that may exhibit a large amount of noise or drift.

AFM kymographs are a valuable method for probing the dynamics of individual membrane proteins but can contain artifacts (Fig. 10). Reduction of the scanning dimension increases time resolution to allow clear observation of conformational transitions, even without a high-speed instrument. By comparing kymograph analyses across two distinct membrane proteins, we demonstrate that an experimenter must consider factors such as conformational behavior, drift, and protein geometry. AFM simulations of protein states allow an experimenter to

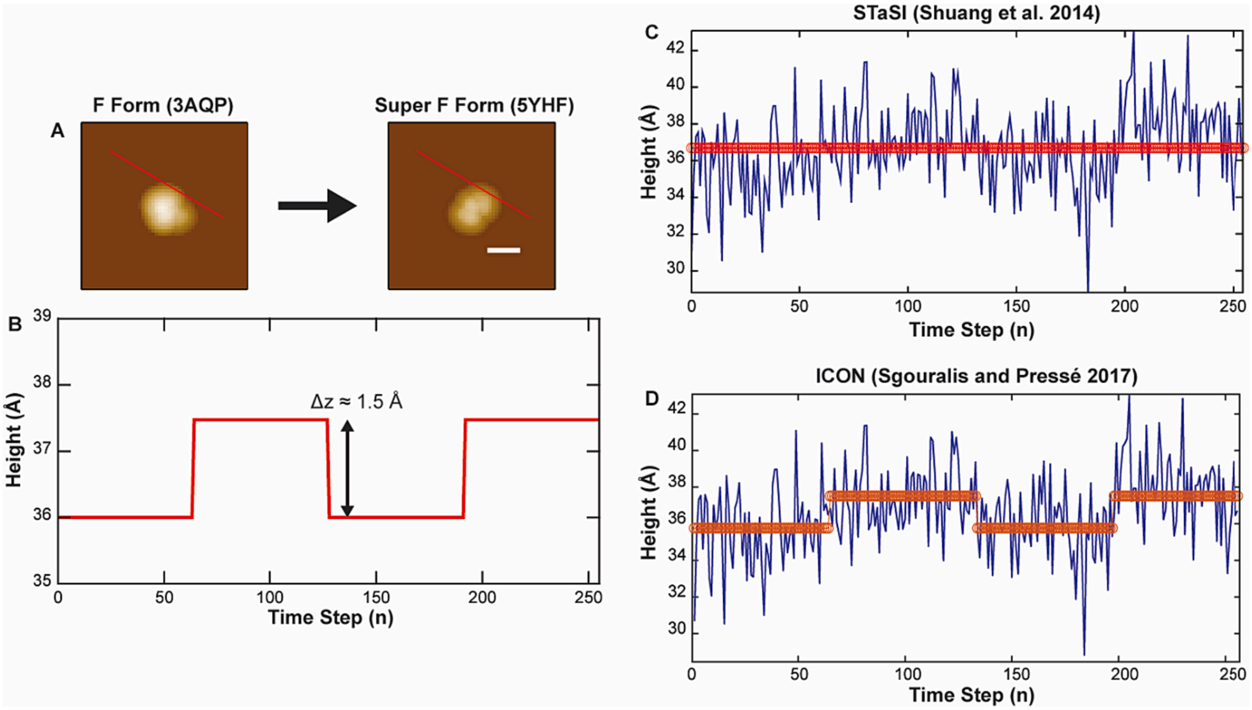

Fig. 9. Improved algorithm for accurate state detection in the presence of noise. (A) Simulated AFM images of SecDF in two states are shown with a line scan going through the same nominal location: 30° scan angle, 7 nm drift from the center of mass. (B) Simulated kymograph data was produced at the line scan locations. Note the height change Δz between the states is below the typical noise level. Upon addition of 2 Å Gaussian noise, the resulting state identification output is given for (C) STaSI and (D) ICON. We see that the iHMM procedure in ICON identifies the two conformations whereas STaSI does not.

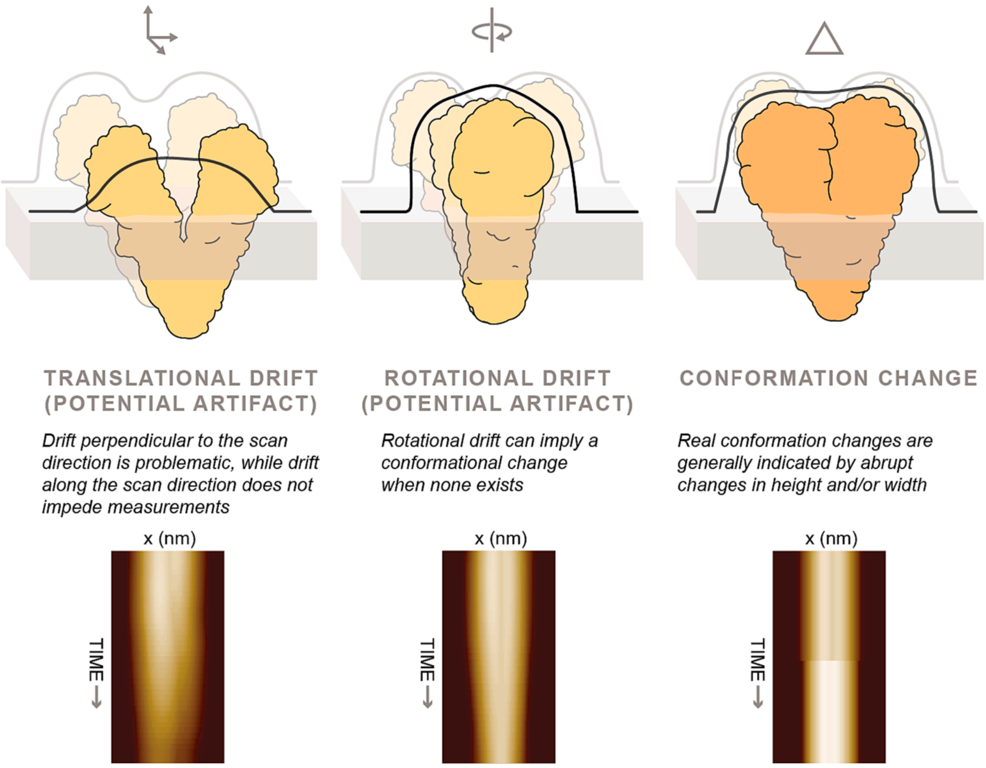

Fig. 10. Summary Cartoon. Translational or rotational drift can result in changes in height or width. If drift occurs on a fast timescale (i.e., faster than the kymograph scan rate), these can result in artifactual transitions. Cartoons illustrate both drift modalities contrasted with a true conformational change. Simulated kymographs demonstrate the gradual progression characteristic of drift (bottom row: left & middle). An abrupt transition (bottom row: right) is more likely to arise from a real conformational change occurring on a timescale similar to or below the scanning period.

determine the limitations of their system for both lateral and rotational drift. For Pgp and SecDF, we found that a lateral drift of 5 nm, or ~ 50 % of the protein radius, was sufficient for high (>92 %) transition detection confidence. Based on the typical drift rates observed in our instrument, a kymograph lasting 25 s is acceptable for analysis, though a more conservative user can reduce this length for higher accuracy. By quantifying the amount of drift that can be allowed for a protein of interest during an experiment without introducing artifacts, one acquire kymographs that stay within the acceptable drift margin for the quantity being measured. Several analysis methods based on robust statistical foundations are available to fit traces extracted from an AFM kymograph, enabling accurate state transition detection and the associated kinetics. Careful AFM kymograph analyses are poised to further understanding of membrane protein dynamics in near-native conditions.

Declaration of competing interest

The authors declare that they have no known competing financial interests or personal relationships that could have appeared to influence the work reported in this paper.

Data availability

Data will be made available on request.

Acknowledgements

This work was supported by the National Science Foundation (2122027, to G.M.K.). K.G.S. acknowledges support from the Research Excellence Program (REP) at the University of Missouri.

References

[1] A.A. Kermani, A guide to membrane protein X-ray crystallography, FEBS J. 288 (2021) 5788–5804.
[2] C.-Y. Huang, V. Olieric, P. Ma, E. Panepucci, K. Diederichs, M. Wang, M. Caffrey, In meso in situ serial X-ray crystallography of soluble and membrane proteins, Acta Crystallogr. D Biol. Crystallogr. 71 (2015) 1238–1256.
[3] M.S. Hunter, D.P. DePonte, D.A. Shapiro, R.A. Kirian, X. Wang, D. Starodub, S. Marchesini, U. Weierstall, R.B. Doak, J.C.H. Spence, P. Fromme, X-ray Diffraction from Membrane Protein Nanocrystals, Biophys. J . 100 (2011) 198–206.
[4] P.K. Fyfe, K.E. McAuley, A.W. Roszak, N.W. Isaacs, R.J. Cogdell, M.R. Jones, Probing the interface between membrane proteins and membrane lipids by X-ray crystallography, Trends Biochem. Sci 26 (2001) 106–112.
[5] S.H.W. Scheres, RELION: Implementation of a Bayesian approach to cryo-EM structure determination, J. Struct. Biol. 180 (2012) 519–530.
[6] M. Liao, E. Cao, D. Julius, Y. Cheng, Structure of the TRPV1 ion channel determined by electron cryo-microscopy, Nature 504 (2013) 107–112.
[7] Passmore, L. A., and Russo, C. J. (2016) Chapter Three - Specimen Preparation for High-Resolution Cryo-EM. in *Methods in Enzymology* (Crowther, R. A. ed), pp. 51–86, The Resolution Revolution: Recent Advances In cryoEM, Academic Press, **579**, 51–86.
[8] Y. Cheng, Membrane protein structural biology in the era of single particle cryo-EM, Curr. Opin. Struct. Biol. 52 (2018) 58–63.
[9] C.A. Bippes, D.J. Muller, High-resolution atomic force microscopy and spectroscopy of native membrane proteins, Rep. Prog. Phys. 74 (2011) 086601.
[10] D.J. Müller, A. Engel, Atomic force microscopy and spectroscopy of native membrane proteins, Nat. Protoc. 2 (2007) 2191–2197.
[11] A. Alessandrini, P. Facci, AFM: a versatile tool in biophysics, Meas. Sci. Technol. 16 (2005) R65.
[12] T. Ando, N. Kodera, E. Takai, D. Maruyama, K. Saito, A. Toda, A high-speed atomic force microscope for studying biological macromolecules, Proc. Natl. Acad. Sci. 98 (2001) 12468–12472.
[13] T. Ando, High-speed atomic force microscopy and its future prospects, Biophys. Rev. 10 (2018) 285–292.
[14] N. Kodera, D. Yamamoto, R. Ishikawa, T. Ando, Video imaging of walking myosin V by high-speed atomic force microscopy, Nature 468 (2010) 72–76.
[15] A. Miyagi, C. Chipot, M. Rangl, S. Scheuring, High-speed atomic force microscopy shows that annexin V stabilizes membranes on the second timescale, Nat. Nanotechnol. 11 (2016) 783–790.

[16] N. Chada, K. Chattrakun, B.P. Marsh, C. Mao, P. Bariya, G.M. King, Single-molecule observation of nucleotide induced conformational changes in basal SecA-ATP hydrolysis, Sci. Adv. 4 (2018) eaat8797.

[17] G.J. Stanley, B. Akpinar, Q. Shen, P.D.E. Fisher, C.P. Lusk, C. Lin, B. W. Hoogenboom, Quantification of biomolecular dynamics inside real and synthetic nuclear pore complexes using time-resolved atomic force microscopy, ACS Nano 13 (2019) 7949–7956.

[18] A.P. Perrino, A. Miyagi, S. Scheuring, Single molecule kinetics of bacteriorhodopsin by HS-AFM, Nat. Commun. 12 (2021) 7225.

[19] S. Maity, G. Trinco, P. Buzón, Z.R. Anshari, N. Kodera, K.X. Ngo, T. Ando, D. J. Slotboom, W.H. Roos, High-speed atomic force microscopy reveals a three-state elevator mechanism in the citrate transporter CitS, Proc. Natl. Acad. Sci. 119 (2022) e2113927119.

[20] R.R. Sanganna Gari, N.C. Frey, C. Mao, L.L. Randall, G.M. King, Dynamic Structure of the Translocon SecYEG in Membrane: Direct Single Molecule Observations, J. Biol. Chem. 288 (2013) 16848–16854.

[21] D.R. Weaver, D.N. Amin, G.M. King, The conformations and basal conformational dynamics of translocation factor SecDF vary with translocon SecYEG interaction, J. Biol. Chem. (2022), https://doi.org/10.1016/j.jbc.2022.102412.

[22] D.R. Weaver, G.M. King, Atomic Force Microscopy Reveals Complexity Underlying General Secretory System Activity, Int. J. Mol. Sci. 24 (2023) 55.

[23] R.R. Sanganna Gari, K. Chattrakun, B.P. Marsh, C. Mao, N. Chada, L.L. Randall, G. M. King, Direct visualization of the E. coli Sec translocase engaging precursor proteins in lipid bilayers, Sci. Adv. 5 (2019) eaav9404.

[24] G.M. King, A.R. Carter, A.B. Churnside, L.S. Eberle, T.T. Perkins, Ultrastable Atomic Force Microscopy: Atomic-Scale Stability and Registration in Ambient Conditions, Nano Lett. 9 (2009) 1451–1456.

[25] K.G. Schaefer, A.G. Roberts, G.M. King, Advantages and potential limitations of applying AFM kymograph analysis to pharmaceutically relevant membrane proteins in lipid bilayers, Sci. Rep. 13 (2023) 11427.

[26] K.P. Sigdel, L.A. Wilt, B.P. Marsh, A.G. Roberts, G.M. King, The conformation and dynamics of P-glycoprotein in a lipid bilayer investigated by atomic force microscopy, Biochem. Pharmacol. 156 (2018) 302–311.

[27] P.H. Nguyen, K.P. Sigdel, K.G. Schaefer, G.A.K. Mensah, G.M. King, A.G. Roberts, The effects of anthracycline drugs on the conformational distribution of mouse P-glycoprotein explains their transport rate differences, Biochem. Pharmacol. 174 (2020) 113813.

[28] T. Tsukazaki, H. Mori, Y. Echizen, R. Ishitani, S. Fukai, T. Tanaka, A. Perederina, D. G. Vassylyev, T. Kohno, A.D. Maturana, K. Ito, O. Nureki, Structure and function of a membrane component SecDF that enhances protein export, Nature 474 (2011) 235–238.

[29] R. Arkowitz, W. Wickner, SecD and SecF are required for the proton electrochemical gradient stimulation of preprotein translocation, EMBO J. 13 (1994) 954–963.

[30] T. Tsukazaki, Structure-based working model of SecDF, a proton-driven bacterial protein translocation factor, FEMS Microbiol. Lett. (2018), https://doi.org/10.1093/femsle/fny112.

[31] B.P. Marsh, N. Chada, R.R. Sanganna Gari, K.P. Sigdel, G.M. King, The Hessian Blob Algorithm: Precise Particle Detection in Atomic Force Microscopy Imagery, Sci. Rep. 8 (2018) 1–12.

[32] A. Moeller, S.C. Lee, H. Tao, J.A. Speir, G. Chang, I.L. Urbatsch, C.S. Potter, B. Carragher, Q. Zhang, Distinct Conformational Spectrum of Homologous Multidrug ABC Transporters, Structure 23 (2015) 450–460.

[33] M.J. Li, M. Guttman, W.M. Atkins, Conformational dynamics of P-glycoprotein in lipid nanodiscs and detergent micelles reveal complex motions on a wide time scale, J. Biol. Chem. 293 (2018) 6297–6307.

[34] Q. Qu, F.J. Sharom, FRET Analysis Indicates That the Two ATPase Active Sites of the P-Glycoprotein Multidrug Transporter Are Closely Associated, Biochemistry 40 (2001) 1413–1422.

[35] A.B. Ward, P. Szewczyk, V. Grimard, C.-W. Lee, L. Martinez, R. Doshi, A. Caya, M. Villaluz, E. Pardon, C. Cregger, D.J. Swartz, P.G. Falson, I.L. Urbatsch, C. Govaerts, J. Steyaert, G. Chang, Structures of P-glycoprotein reveal its conformational flexibility and an epitope on the nucleotide-binding domain, Proc. Natl. Acad. Sci. 110 (2013) 13386–13391.

[36] K. Chattrakun, K.G. Schaefer, L.S. Chandler, B.P. Marsh, G.M. King, Atomic force microscopy reveals membrane protein activity at the single molecule level, in: I. Schmidt-Krey, J.C. Gumbart (Eds.), Structure and Function of Membrane Proteins, Springer, US, New York, NY, 2021, pp. 81–99, https://doi.org/10.1007/978-1-0716-1394-8_6. Methods in Molecular Biology.

[37] B.J. Berne, R. Pecora, Dynamic Light Scattering: With Applications to Chemistry, Biology, and, Physics, Courier Corporation, 2000.

[38] G.R. Bartlett, Phosphorus assay in column chromatography, J. Biol. Chem. 234 (1959) 466–468.

[39] N. Chada, K.P. Sigdel, R.R.S. Gari, T.R. Matin, L.L. Randall, G.M. King, Glass is a viable substrate for precision force microscopy of membrane proteins, Sci. Rep. 5 (2015) 12550.

[40] S. Takeda, K. Yamamoto, Y. Hayasaka, K. Matsumoto, Surface OH group governing wettability of commercial glasses, J. Non Cryst. Solids 249 (1999) 41–46.

[41] B. Shuang, D. Cooper, J.N. Taylor, L. Kisley, J. Chen, W. Wang, C.B. Li, T. Komatsuzaki, C.F. Landes, fast step transition and state identification (STaSI) for discrete single-molecule data analysis, J. Phys. Chem. Lett. 5 (2014) 3157–3161.

[42] J. Rissanen, A universal prior for integers and estimation by minimum description length, Ann. Stat. 11 (1983) 416–431.

[43] A. Barbieri, N. Thonghin, T. Shafi, S.M. Prince, R.F. Collins, R.C. Ford, Structure of ABCB1/P-glycoprotein in the presence of the CFTR potentiator ivacaftor, Membranes 11 (2021) 923.

[44] Y. Kim, J. Chen, Molecular structure of human P-glycoprotein in the ATP-bound, outward-facing conformation, Science 359 (2018) 915–919.

[45] A. Furukawa, S. Nakayama, K. Yoshikaie, Y. Tanaka, T. Tsukazaki, Remote coupled drastic β-barrel to β-sheet transition of the protein translocation motor, Structure 26 (2018) 485–489.e2.

[46] S. Alvarez, A cartography of the van der Waals territories, Dalton Trans. 42 (2013) 8617–8636.

[47] M.A. Lomize, I.D. Pogozheva, H. Joo, H.I. Mosberg, A.L. Lomize, OPM database and PPM web server: resources for positioning of proteins in membranes, Nucleic Acids Res. 40 (2012) D370–D376.

[48] K.G. Schaefer, A.E. Pittman, F.N. Barrera, G.M. King, Atomic force microscopy for quantitative understanding of peptide-induced lipid bilayer remodeling, Methods (2020), https://doi.org/10.1016/j.ymeth.2020.10.014.

[49] G.A. Frank, S. Shukla, P. Rao, M.J. Borgnia, A. Bartesaghi, A. Merk, A. Mobin, L. Esser, L.A. Earl, M.M. Gottesman, D. Xia, S.V. Ambudkar, S. Subramaniam, Cryo-EM Analysis of the Conformational Landscape of Human P-glycoprotein (ABCB1) During its Catalytic Cycle, Mol. Pharmacol. 90 (2016) 35–41.

[50] N. Kopcho, G. Chang, E.A. Komives, Dynamics of ABC Transporter P-glycoprotein in Three Conformational States, Sci. Rep. 9 (2019) 15092.

[51] B. Verhalen, S. Ernst, M. Börsch, S. Wilkens, Dynamic ligand-induced conformational rearrangements in P-glycoprotein as probed by fluorescence resonance energy transfer spectroscopy, J. Biol. Chem. 287 (2012) 1112–1127.

[52] Z.E. Sauna, I.-W. Kim, K. Nandigama, S. Kopp, P. Chiba, S.V. Ambudkar, Catalytic Cycle of ATP Hydrolysis by P-Glycoprotein: Evidence for Formation of the E·S Reaction Intermediate with ATP-γ-S, a Nonhydrolyzable Analogue of ATP, Biochemistry 46 (2007) 13787–13799.

[53] T.R. Matin, G.R. Heath, G.H.M. Huysmans, O. Boudker, S. Scheuring, Millisecond dynamics of an unlabeled amino acid transporter, Nat. Commun. 11 (2020) 5016.

[54] S.J. Singer, G.L. Nicolson, The Fluid Mosaic Model of the Structure of Cell Membranes, Science 175 (1972) 720–731.

[55] P.G. Saffman, M. Delbrück, Brownian motion in biological membranes, Proc. Natl. Acad. Sci. 72 (1975) 3111–3113.

[56] N.J.P. Ryba, D. Marsh, Protein rotational diffusion and lipid/protein interactions in recombinants of bovine rhodopsin with saturated diacylphosphatidylcholines of different chain lengths studied by conventional and saturation-transfer electron spin resonance, Biochemistry 31 (1992) 7511–7518.

[57] M. Vögele, J. Köfinger, G. Hummer, Finite-Size-Corrected Rotational Diffusion Coefficients of Membrane Proteins and Carbon Nanotubes from Molecular Dynamics Simulations, J. Phys. Chem. B 123 (2019) 5099–5106.

[58] M. Javanainen, O.H.S. Ollila, H. Martinez-Seara, Rotational Diffusion of Membrane Proteins in Crowded Membranes, J. Phys. Chem. B 124 (2020) 2994–3001.

[59] K. Chattrakun, D.P. Hoogerheide, C. Mao, L.L. Randall, G.M. King, Protein Translocation Activity in Surface-Supported Lipid Bilayers, Langmuir 35 (2019) 12246–12256.

[60] J. Canet-Ferrer, E. Coronado, A. Forment-Aliaga, E. Pinilla-Cienfuegos, Correction of the tip convolution effects in the imaging of nanostructures studied through scanning force microscopy, Nanotechnology 25 (2014) 395703.

[61] M.E. Fuentes-Perez, M.S. Dillingham, F. Moreno-Herrero, AFM volumetric methods for the characterization of proteins and nucleic acids, Methods 60 (2013) 113–121.

[62] A.T. Winzer, C. Kraft, S. Bhushan, V. Stepanenko, I. Tessmer, Correcting for AFM tip induced topography convolutions in protein–DNA samples, Ultramicroscopy 121 (2012) 8–15.

[63] K.E. Hines, A Primer on Bayesian Inference for Biophysical Systems, Biophys. J . 108 (2015) 2103–2113.

[64] K.E. Hines, J.R. Bankston, R.W. Aldrich, Analyzing single-molecule time series via nonparametric Bayesian inference, Biophys. J. 108 (2015) 540–556.

[65] I. Sgouralis, S. Pressé, ICON: An adaptation of infinite HMMs for time traces with drift, Biophys. J. 112 (2017) 2117–2126.

[66] I. Sgouralis, S. Pressé, An introduction to infinite HMMs for single-molecule data analysis, Biophys. J. 112 (2017) 2021–2029.